

Video-rate computational super-resolution and integral imaging at longwave-infrared wavelengths

MIGUEL A. PRECIADO, GUILLEM CARLES, AND ANDREW R. HARVEY*

School of Physics and Astronomy, University of Glasgow, Glasgow G12 8QQ, UK
**andy.harvey@glasgow.ac.uk*

Abstract: We report the first computational super-resolved, multi-camera integral imaging at long-wave infrared (LWIR) wavelengths. A synchronized array of FLIR Lepton cameras was assembled, and computational super-resolution and integral-imaging reconstruction employed to generate video with light-field imaging capabilities, such as 3D imaging and recognition of partially obscured objects, while also providing a four-fold increase in effective pixel count. This approach to high-resolution imaging enables a fundamental reduction in the track length and volume of an imaging system, while also enabling use of low-cost lens materials.

References and links

1. E. Y. Lam, "Computational photography: advances and challenges," *Proc. SPIE* 8122, 81220O (2011).
2. D. R. Gerwe, A. Harvey, and M. E. Gehm, "Computational optical sensing and imaging: Introduction to feature issue," *Appl. Opt.* **52**, COS11–COS12 (2013)
3. Edmund Y. Lam, "Computational photography with plenoptic camera and light field capture: tutorial," *J. Opt. Soc. Am. A* **32**, 2021-2032 (2015)
4. E. H. Adelson and J. Y. A. Wang, "Single lens stereo with a plenoptic camera," *IEEE Transactions on Pattern Analysis and Machine Intelligence*, **14**(2), 99-106 (1992)
5. R. Ng, M. Levoy, M. Brédif, G. Duval, M. Horowitz, and P. Hanrahan, "Light field photography with a hand-held plenoptic camera," *Tech. Rep. CSTR 2005-02* (Stanford University Computer Science Department, 2005).
6. R. Ng, "Digital light field photography," *Ph.D. thesis* (Stanford University, 2006)
7. T. Georgiev and A. Lumsdaine, "Focused plenoptic camera and rendering," *J. Electron. Imaging* **19**, 021106 (2000)
8. M. G. Lippmann, "Épreuves réversibles. Photographies intégrales," *Comptes Rendus de l'Académie des Sciences*. **146**, 446–451 (1908)
9. X. Xiao, B. Javidi, M. Martinez-Corral, and A. Stern, "Advances in three-dimensional integral imaging: sensing, display, and applications [Invited]," *Appl. Opt.* **52**, 546-560 (2013)
10. B. Javidi, I. Moon, and S. Yeom, "Three-dimensional identification of biological microorganism using integral imaging," *Opt. Express* **14**, 12096-12108 (2006)
11. M. Levoy, Z. Zhang, and I. McDowall, "Recording and controlling the 4D light field in a microscope using microlens arrays" *Journal of Microscopy*, **235**(2), 144-162 (2009).
12. S. H. Hong and B. Javidi, "Distortion-tolerant 3D recognition of occluded objects using computational integral imaging," *Opt. Express* **14**, 12085-12095 (2006)
13. M. Daneshpanah and B. Javidi, "Profilometry and optical slicing by passive three-dimensional imaging," *Opt. Lett.* **34**, 1105-1107 (2009)
14. S. Komatsu, A. Markman, A. Mahalanobis, K. Chen, and B. Javidi, "Three-dimensional integral imaging and object detection using long-wave infrared imaging," *Appl. Opt.* **56**, D120-D126 (2017)
15. S. C. Park, M. K. Park, and M. G. Kang, "Super-resolution image reconstruction: a technical overview," *IEEE Signal Process. Mag.* 20(3), 21 (2003).
16. S. S. Young and R. G. Driggers, "Superresolution image reconstruction from a sequence of aliased imagery," *Appl. Opt.* **45**, 5073 (2006)
17. M. Elad and A. Feuer, "Restoration of a single superresolution image from several blurred, noisy, and undersampled measured images," *IEEE Trans. Image Process.* 6, 1646-1658(1997).
18. J. Downing, E. Findlay, G. Muyo, and A. R. Harvey, "Multichanneled finite-conjugate imaging," *J. Opt. Soc. Am. A* **29**, 921-927 (2012)
19. G. Carles, J. Downing, and A. R. Harvey, "Super-resolution imaging using a camera array," *Opt. Lett.* **39**, 1889-1892 (2014)
20. G. Carles, G. Muyo, N. Bustin, A. Wood, and A. R. Harvey, "Compact multi-aperture imaging with high angular resolution," *J. Opt. Soc. Am. A* **32**, 411-419 (2015)
21. T. E. Bishop, S. Zanetti, and P. Favaro, "Light field superresolution," in *IEEE International Conference on Computational Photography*, (2009)

22. T. Bishop and P. Favaro, "The light field camera: extended depth of field, aliasing and super-resolution," *IEEE Trans. Pattern Anal. Mach. Intell.* **34**, 972–986 (2012)
23. H. Kim, S. Lee, T. Ryu, and J. Yoon, "Superresolution of 3-D computational integral imaging based on moving least square method," *Opt. Express* **22**, 28606–28622 (2014)
24. C. Yang, J. Wang, A. Stern, S. Gao, V. Gurev, and B. Javidi, "Three-Dimensional Super Resolution Reconstruction by Integral Imaging," *J. Display Technol.* **11**, 947–952 (2015)
25. T. Grulois, G. Druart, N. Guérineau, A. Crastes, H. Sauer, and P. Chavel, "Extra-thin infrared camera for low-cost surveillance applications," *Opt. Lett.* **39**, 3169–3172 (2014)
26. A. Rogalski, P. Martyniuk, and M. Kopytko, "Challenges of small-pixel infrared detectors: a review," *Rep. Prog. Phys.* **79**, 046501–43 (2016).
27. International Standard ISO 12233:2000(E)
28. Z. Zhang, "A Flexible New Technique for Camera Calibration," *IEEE Transactions on Pattern Analysis and Machine Intelligence.* **22**, 1330–1334 (2000)
29. Heikkilä, J. and O. Silven. "A Four-step Camera Calibration Procedure with Implicit Image Correction." in *IEEE International Conference on Computer Vision and Pattern Recognition*, (1997)
30. S. Thiele, K. Arzenbacher, and T. Gissibl, "3D-printed eagle eye: Compound microlens system for foveated imaging," *Science Advances* **3**, e1602655 (2017)

1. Introduction

Multi-aperture computational imaging [1–3] is of increasing importance in imaging science and consumer products, such as light-field cameras [3–7] and the simpler multiple-camera imaging found in the latest generation of consumer smart phones. Multiple-camera light-field imaging involves imaging from multiple viewpoints and is a special case of the more general concept of computational integral-imaging reconstruction (CIIR) based on concepts originally proposed in 1908 by Gabriel Lippmann [8]. It has great potential for 3D imaging [9] in general, but particularly for medical imaging [10,11], recognition of occluded objects [12] and ranging of targets [13]. CIIR has recently been demonstrated in the long-wave infrared (LWIR) band using a single-camera emulation of a multi-aperture CIIR system [14].

We report the first demonstrations of both multi-camera computational super resolution and of multi-camera integral imaging in the LWIR. Super-resolution imaging can also be achieved by time-sequential processing of video sequences from a single camera [16–17] but the associated time delay is a severe limitation for real-time operation. We have demonstrated the required video-rate hardware synchronization of a camera array and of sub-pixel, multi-camera calibration procedures [21–24] for real-time operation. This technique is made practical by the recent availability of low-cost, low-resolution, LWIR cameras: hitherto camera arrays in the LWIR have been prohibitively expensive.

An important advantage of the down-scaling of lens dimensions for use with these small focal-plane arrays (FPA) is the higher optical transmission of the thinner lenses. Imaging systems based on camera arrays may thus employ higher-loss lens materials such as silicon or polyethylene, enabling low-cost manufacture using molding or photolithography [25]. Figure 1 shows a comparison of the variation in the optical transmission (averaged across the LWIR band), as a function of focal length for representative, germanium and silicon $f/1$ and $f/2$ doublet lenses. The lenses were individually optimized and modelled in *Zemax*. It can be seen that while the more expensive germanium lenses exhibit high transmission for a wide range of focal lengths, the absorption for a silicon doublet $f/1$ lens is a low 3% (in addition to reflection losses from the four anti-reflection coated surfaces) for a focal length of 3mm, but increases strongly with focal length reaching about 25% for a focal length of 10mm.

For fast optics, as are typically used in uncooled thermal imaging, the angular resolution is limited not by diffraction, but by pixel size. The 17- μm pixel size of the FLIR *Lepton* cameras used here is almost twice the size of the point-spread function and introduces significant aliasing providing good scope for resolution enhancement using super resolution. The pixel size of LWIR cameras continues to reduce with improvements in manufacturing technology, progressively eroding the benefits that may be attainable from SR. In Fig. 2(a) we show calculated system MTFs for several pixel sizes for a diffraction-limited, $f/1$, LWIR-band imaging system, normalized to the sampling frequency (the reciprocal of the pixel width,

assuming a 100% fill factor) and in (b) we show the MTF at the Nyquist frequency as a function of pixel size. It can be appreciated that there is continued scope for enhancement in spatial resolution using SR for pixel sizes greater than 5 μm . The emerging generation of uncooled LWIR detector arrays have 12- μm pixels and there is no clear timescale for reduction in pixel size to 5 μm [26], even though extrapolation of current trends, consequently SR offers scope for enhanced resolution and reduction in camera size for the foreseeable future. In these circumstances the three fundamental advantages of a multi-camera array for generating images with space-bandwidth products of tens of thousands of pixels: are the exploitation of SR to reduce track length of optics [18-20], the possibility of using low-cost silicon and polyethylene lenses and for the additional multi-functional capabilities of integral imaging as described below. Conventionally, pixel counts this large would be achieved with a single larger FPA and a single longer focal length, higher cost, germanium lens.

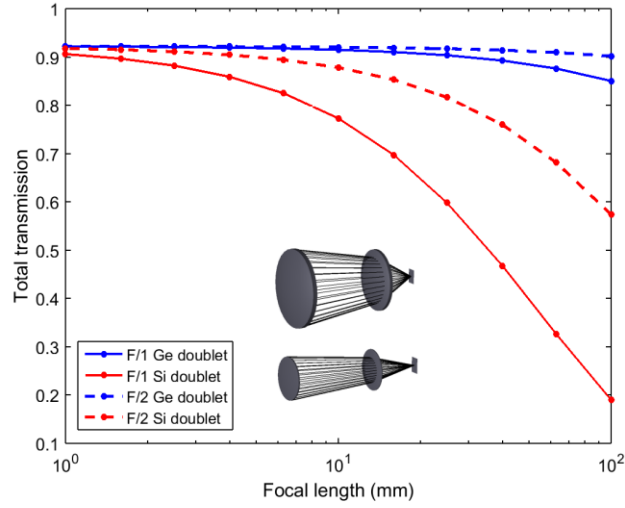


Figure 1. Calculated variation of optical transmission with focal length for anti-reflection coated silicon and germanium doublet lenses.

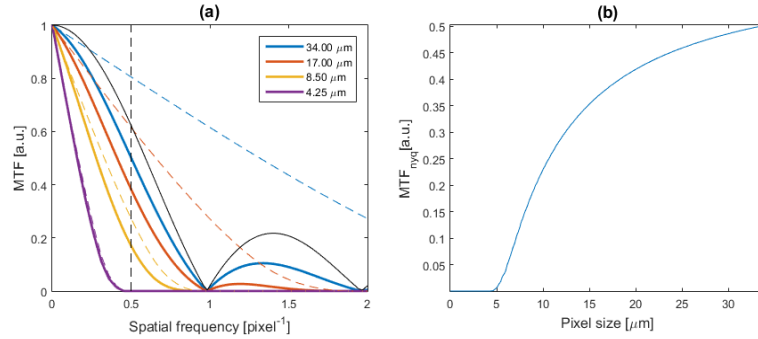


Figure 2. Analysis of computational SR in the LWIR for a range of pixel sizes. Subplot (a) shows system MTF as a function of pixel size, where: the Nyquist frequency is indicated by a vertical dashed black line, the pixel MTF is shown by a black-solid line, the optics MTF is shown by the colored dashed lines, and the overall MTF indicated by colored solid lines. Subplot (b) indicates the overall MTF at the Nyquist frequency (MTF_{nyq}) as a function of pixel size.

We describe below the calibration and synchronization of an array of low-cost uncooled LWIR cameras (FLIR *Lepton*). We confirm that the lenses are sufficiently well corrected to enable enhanced image resolution through SR (that is, there is strong aliasing) and describe the

sub-pixel calibration of the camera array and the computational image reconstruction for simultaneous CIIR-SR. We then discuss some example applications: demonstrating a clear improvement of the effective resolution by computational SR; showing also volumetric, super-resolved, 3D reconstruction of video sequences.

2. Optical characterization, calibration and image construction.

Our demonstration system employs an array of six synchronized LWIR cameras based on compact, low-cost FLIR® *Lepton*® cameras, which employ a focal-plane array of 80x60 active 17- μm pixels and a silicon doublet lens with a focal length of 3 mm, yielding a 25° horizontal field of view. The cameras are arranged in a 2x3 array with a 27x33 mm cell size as shown in Fig. 2 (a). Each camera is controlled by a dedicated single-board computer (*Raspberry Pi 2B*) interfaced via Ethernet to a personal computer. The synchronization of the system is achieved by a combination of a broadcast Ethernet datagram to initiate video capture in all cameras simultaneously and hardware synchronization of the individual camera clocks at the beginning of every video sequence. Following calibration of the camera array we obtain a multi-functional camera-array with 3D-imaging capabilities using CIIR, and improved resolution through application of computational SR.

Computational SR allows the recovery of aliased spatial frequencies that fall above the Nyquist frequency of the detector array to yield a higher-resolution image with increased pixel count and increased angular resolution [15-17,19,20]. The selection of six as the number of cameras offers an efficient and pragmatic trade between improvement in linear resolution with increasing camera number and the increasing complexity of the camera-array. In principle, linear resolution is improved by a factor equal to the square root of the number of cameras [18], that is a factor of 2.4; twelve cameras would in principle be required to provide the maximal diffraction-limited factor of 3.4 enhancement. The spatial-frequency response of the pixilated array suppresses the transfer function for higher spatial frequencies however and so the higher spatial frequencies tend to exhibit poorer signal-to-noise ratios *ergo* there is a diminishing advantage from employing additional cameras. An additional consideration is that the relatively low geometrical tolerance for alignment of the cameras results in randomized sampling of spatial phase with some redundancy and so the effective enhancement is expected to be slightly less than the ideal factor of 2.4.

The scope for image enhancement through computational SR is contingent upon the optics being of sufficient quality to exhibit a sufficiently high modulation-transfer function (MTF) above the Nyquist-frequency of the detector array. In Figure 2(b) is shown the calculated MTFs of: the camera optics, the detector and the combined system MTF together with the measured camera spatial-frequency response (SFR). The MTFs are calculated based on the 17- μm pixel size of the FLIR *Lepton* camera, assuming diffraction-limited, $f/1.1$ optics, averaged across the LWIR band (8 to 12 μm wavelength). The SFR has been calculated using the standard slanted-edge methods [27] as an approximation to the MTF and there is good consistency demonstrated between the cameras. The similarity between the measured SFR curves and the calculated system MTF is indicative that the lenses are close to being diffraction limited on axis. The presence of components within the system MTF with significant amplitudes above the Nyquist frequency is indicative that SR could be effective in enhancing spatial resolution.

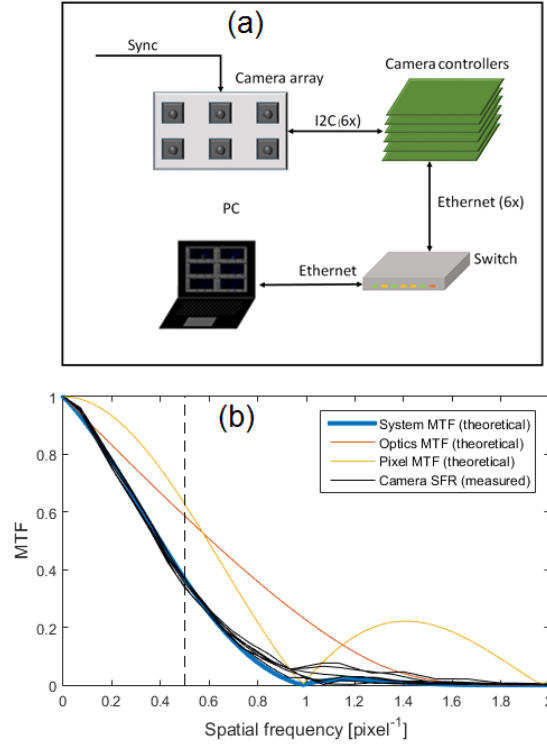


Figure 3(a) Schematic representation of the modular multi-camera array system, (b) the calculated system MTF (blue), with the optical MTF (red), pixel MTF (yellow) and the six measured system SFRs for every (black lines).

Computational SR requires accurate sub-pixel registration of the six images to enable accurate reconstruction of the high-frequency components from the aliased camera images. A direct way to register the images involves finding correspondences between features that are matched between camera images, and using that information to perform the rectification and registration of the images [19], but this is impractical here because of the low pixel count of the cameras. We have employed instead CIIR in combination with SR to perform the image registration. To this end we have performed an accurate multi-camera calibration (see Fig. 4) using images of calibration targets at a variety of object positions to deduce intrinsic parameters for each camera (magnification and distortion), as well as the extrinsic parameters (geometrical model of the camera array). The calibration procedure includes two steps: In the first step a standard calibration of each camera pair [28, 29] yields the extrinsic and intrinsic parameters. A target providing well-defined loci is required for this calibration, and for visible-band imaging a chessboard pattern is usually employed. We have adapted this method for the LWIR band by using a 3D-printed pattern composed of a square array of holes, back-illuminated by a heated surface. In a second calibration step we improve the accuracy of the calibration by using similar patterns at specific distances and correct the previously obtained extrinsic parameters to match the disparity/distance relation between all the camera pairs.

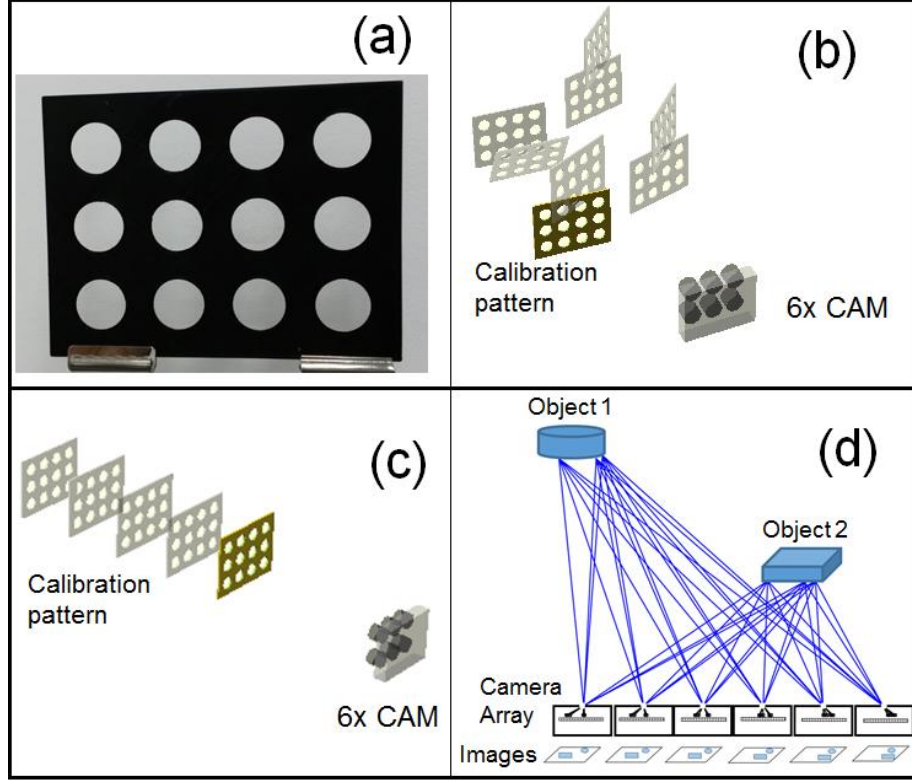


Figure 4. Calibration process: (a) a visible-light photograph of a 3D-printed plastic calibration target. (b) Step 1: the back-illuminated calibration target is imaged by the camera array at various positions and orientations (c) Step 2: the sub-pixel accuracy required for SR is improved by imaging the pattern at controlled distances. Subplot (d) illustrates the ray diagram detection of the camera array (pinhole model), which can be numerically retraced by CIIR after calibration.

After this calibration, the images are registered at a specific distance from the reference camera with sufficient accuracy to perform computational SR based on the approximation provided by our CIIR. From the calibration parameters obtained, the relation between the coordinates of camera k and the reference camera are given by:

$$\begin{bmatrix} u_k \\ v_k \\ w_k \end{bmatrix} = \mathbf{H}_{k,z} \begin{bmatrix} x_1 \\ y_1 \\ 1 \end{bmatrix} \quad (1)$$

$$x_k = x_k(x_1, y_1, z_1) = u_k / w_k \quad (2)$$

$$y_k = y_k(x_1, y_1, z_1) = v_k / w_k \quad (3)$$

where $k=2,3,...,N_{\text{cam}}$, N_{cam} is the number of cameras (=6 here) and $k=1$ refers to the reference camera. The 3x3 homography matrices $\mathbf{H}_{k,z}$ can be calculated at a specific distance to the reference camera plane, z :

$$\mathbf{H}_{k,z} = \mathbf{H}_{v,k} + \mathbf{H}_{\text{shift},k} z^{-1} \quad (4)$$

where the components $\mathbf{H}_{v,k}$ and $\mathbf{H}_{\text{shift},k}$ are calculated from the extrinsic parameters deduced in the previous calibration process. The previous equations assume a purely geometric pinhole camera model, which neglects optical distortions. The actual camera coordinates (x'_k, y'_k) can be deduced by using the intrinsic parameters calculated in the calibration process:

$$x'_k = x_{k,0} + (x_k - x_{k,0})(1 + D_{k,1}r^2 + D_{k,2}r^4) \quad (5)$$

$$y'_k = y_{k,0} + (y_k - y_{k,0})(1 + D_{k,1}r^2 + D_{k,2}r^4) \quad (6)$$

$$r = \left(\left((x_k - x_{k,0})/f_{k,x} \right)^2 + \left((y_k - y_{k,0})/f_{k,y} \right)^2 \right)^{1/2} \quad (7)$$

where $D_{k,1}$ and $D_{k,2}$ are the distortion coefficients, $f_{k,x}$ and $f_{k,y}$ are focal-length coefficients, and $x_{k,0}$, $y_{k,0}$ are the coordinates of the optical center, each referred to camera k . One option to solve the computational SR problem is to invert the forward model that describes the image capture,

$$\mathbf{y}_{\text{LR},k} = \mathbf{D}\mathbf{W}_{k,z}\mathbf{y}_{\text{HR}} + \mathbf{e}_k, \quad (8)$$

where \mathbf{y}_{HR} is a lexicographical ordered column vector representing a high-resolution image in the reference-camera coordinates with length N_{HR} , the total number of pixels for the high-resolution image; $\mathbf{y}_{\text{LR},k}$ is a lexicographical ordered column vector representing the camera- k captured low-resolution image in camera- k coordinates with length N_{LR} ; $\mathbf{W}_{k,z}$ is the $N_{\text{HR}} \times N_{\text{HR}}$ warping matrix which effectively performs the image registration by relating the reference camera coordinates to the k camera coordinates; \mathbf{D} is a $N_{\text{LR}} \times N_{\text{HR}}$ matrix implementing a rational decimation operator which emulates the camera pixel detection collecting the intensity of pixel blocks of the high resolution image, effectively performing a down-sampling of the image; and \mathbf{e}_k represents the noise added during image capture. The warping matrices $\mathbf{W}_k(z_1)$ are constructed from the $\mathbf{H}_{k,z}$ matrices obtained in the registration procedure, and effectively project each high-resolution pixel from the coordinate system of the reference camera to that of camera k (after the projection, bilinear interpolation is used within matrix entries to avoid artefacts in the final reconstructed image).

The set of equations defined by Eq. (8) for $k=1, \dots, N_{\text{cam}}$ can be rewritten in a single equation as:

$$\mathbf{y}_{\text{LR}} = \mathbf{M}_z \mathbf{y}_{\text{HR}} + \mathbf{e} \quad (9)$$

where \mathbf{y}_{LR} and \mathbf{e} are column vectors of length $N_{\text{cam}} \times N_{\text{LR}}$ representing the concatenation of all $\mathbf{y}_{\text{LR},k}$ images and \mathbf{e}_k noise column vectors, respectively; and the system matrix $\mathbf{M}(z_1)$ is defined as

$$\mathbf{M}_z = \begin{bmatrix} \mathbf{D}\mathbf{W}_{1,z} \\ \mathbf{D}\mathbf{W}_{2,z} \\ \vdots \\ \mathbf{D}\mathbf{W}_{N_{\text{cam}},z} \end{bmatrix} \quad (10)$$

Computational SR aims to reconstruct the high-resolution image \mathbf{y}_{HR} that leads to the set of captured images $\mathbf{y}_{\text{LR},k}$. Several SR algorithms have been reported, such as non-uniform interpolation, maximum-likelihood estimation, error-reduction energy, maximum *a priori* estimation, and projection into convex sets have been reported [15-17]. Here we have applied a maximum-likelihood estimation [15], commonly used to estimate parameters from noisy data, specifically Richardson-Lucy deconvolution approximation of \mathbf{y}_{HR} by following an iterative process similar to that described in [19]:

$$\mathbf{y}_{\text{HR},n+1} = \text{diag}(\mathbf{y}_{\text{HR},n}) \mathbf{M}_z^T \left(\text{diag}(\mathbf{M} \mathbf{y}_{\text{HR},n}) \right)^{-1} \mathbf{y}_{\text{LR}} \quad (11)$$

where $\mathbf{y}_{\text{HR},n}$ represents the n -th iterative approximation to \mathbf{y}_{HR} , and $\text{diag}(x)$ denotes a diagonal matrix composed of elements of vector x . This iterative process can be applied at different object ranges from the reference camera, leading to a CIIR-SR 3D volumetric reconstruction of the scene with increased effective resolution for the reconstructed image compared to the native resolution of each individual camera at planes where the image is digitally refocused. This is demonstrated by the example images reported in the next section.

3. Results

We have applied the processes described above for registration and CIIR-SR reconstruction for imaging of three scenes: a) resolution targets for a qualitative and quantitative analysis of the resolution improvement achieved by computational SR; b) a static 3D scene composed of objects at various ranges to demonstrate 3D volumetric reconstruction; and c) 4D (that is, three spatial dimensions plus time) video volumetric reconstruction of people at dissimilar ranges.

For the first example, three resolution targets (star pattern, concentric-circles pattern, and a standard USAF-51 target) were 3D printed in plastic (PLA) and back illuminated by a high-emissivity surface. The homogenous background IR radiation was provided by a 2-cm thick, heated aluminium plate coated with high emissivity paint.

In Fig. 5 we present visible-band images of the three test targets in the left-most column, example images from a single LWIR camera module in the center column and SR images constructed from the six low-resolution images in the right column. The SR reconstructions demonstrate an obvious improvement over the native resolution of a single camera module. Values for the contrast transfer function (CTF) taken from the appropriate elements of the USAF-51 targets are shown in Fig 6. As can be observed, the CTF shows significant contrast at the recovered spatial frequencies up to approximately double the Nyquist frequency, improving the effective resolution by an expected factor of approximately 2. It can be appreciated that computational SR not only increases the effective resolution, but also eradicates the undesirable aliasing artefacts.

We further assess the SR imaging performance using the star resolution targets shown in Fig. 7, where the top row depicts the ground-truth target and spectrum, the middle row shows a low-resolution image from a single LWIR module and its spectrum and the SR-reconstructed image and its spectrum are shown in the bottom row. As can be seen from the frequency spectra, the application of SR reconstructs frequency spectra in the SR image, which in the low-resolution image, are aliased into the baseband of frequencies to yield characteristic aliasing artefacts in Fig. 7(b) that are absent in the SR image in Fig. 7(c).

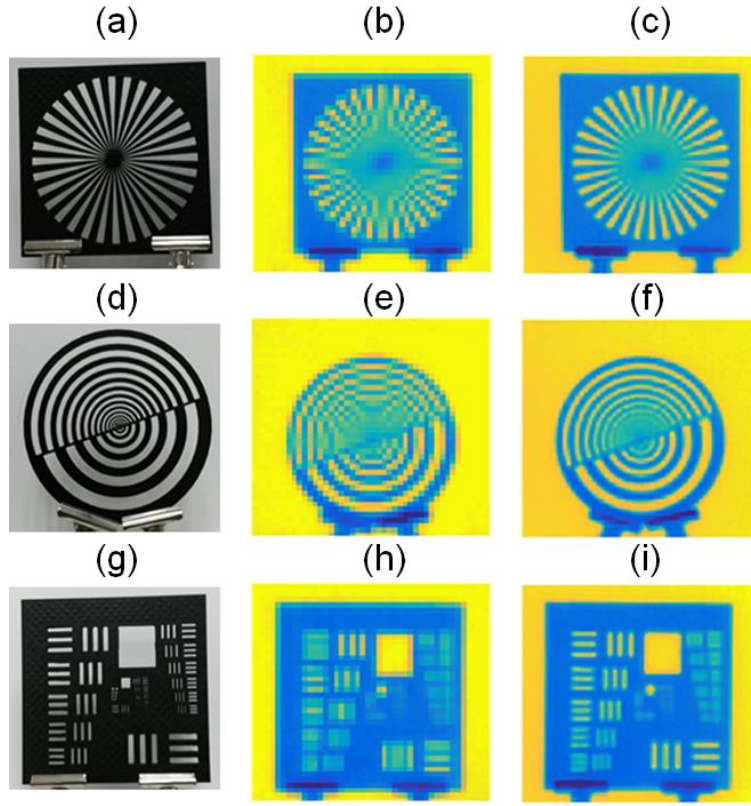


Figure 5. Images of the resolution charts using a visible camera (a), (d), and (g); original low resolution LWIR image captured by the reference camera (b), (e), and (h), and corresponding super-resolved LWIR images in (c), (f), and (i), respectively, for the three different resolution charts.

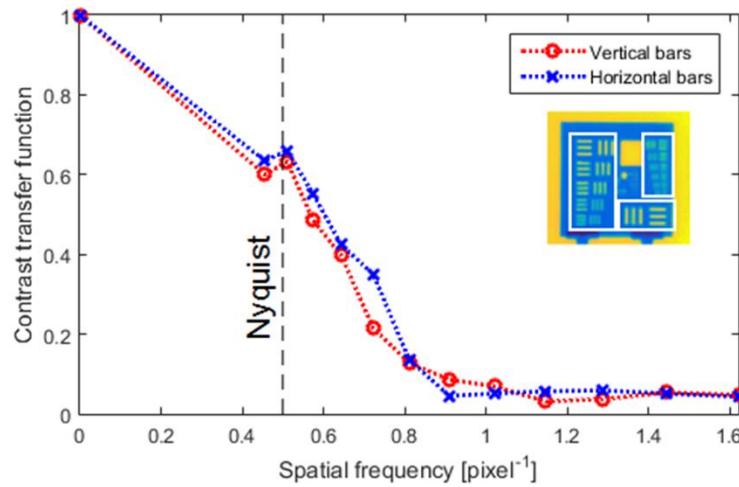


Figure 6. Contrast transfer function (dotted line) measured from the SR image of USAF-51 target for horizontal (blue-crosses) and vertical (red-circles) bar-target elements in the lower row of Figure 4. The Nyquist frequency is indicated by a dashed vertical line.

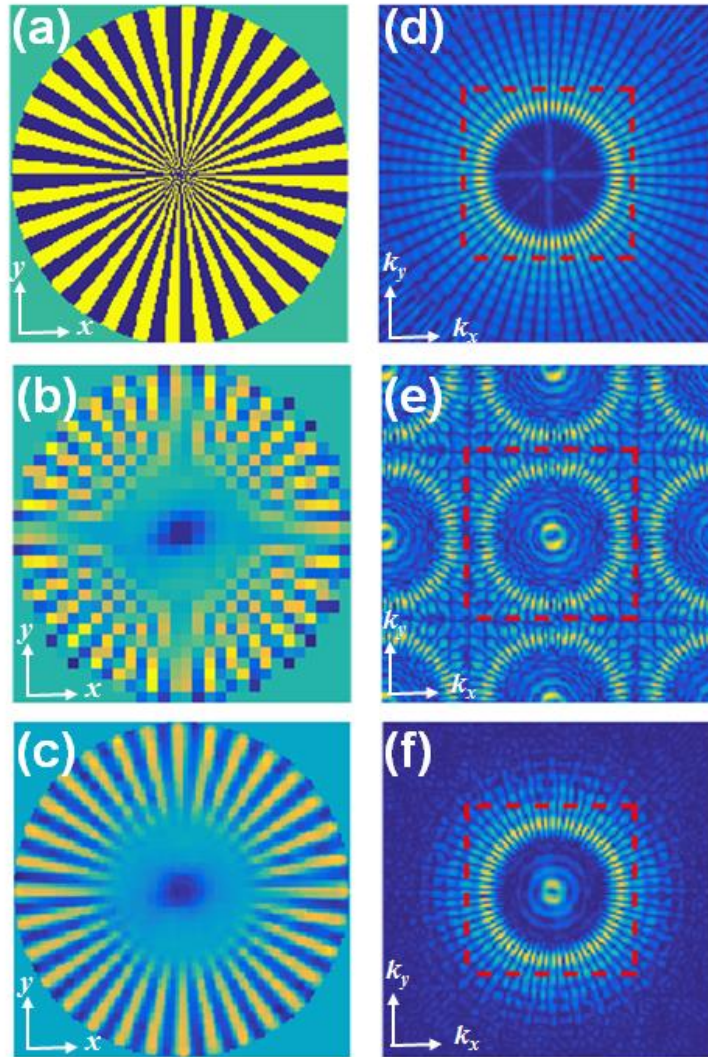


Figure 7. Spatial frequency analysis of SR imaging using the star target. (a) ground truth, (b) a low-resolution image and (c) SR image. (d), (e) and (f) show the respective spatial-frequency spectra, where the horizontal and vertical Nyquist frequency limits are indicated with a dashed red line showing that the aliased high-frequency components in (e) are recovered in the SR image of (f), which has the expected non-aliased, low-pass-filter version of (d)

The simultaneous CIIR-SR capabilities of the system are illustrated in Fig 8. A visible-band image of a 3D scene of model trees and a car is shown in Fig 7(a) and a low-resolution LWIR image is shown in Fig 7(b). Digital refocusing at the ranges of 1.02 m (rear bush), 0.885 m (toy car), and 0.820 m (front bush) shown in (c), (d) and (e) demonstrates digital refocusing and SR on each object. Digital refocusing is a term often used in light field imaging to refer to digital defocus of the images of scene components displaced from a plane of interest; that is, it corresponds to localized reduction in information. The digital refocusing applied here refers to a combination of both SR of the targeted object range, increasing local information content of those scene components, combined with digital defocusing for displaced scene components.

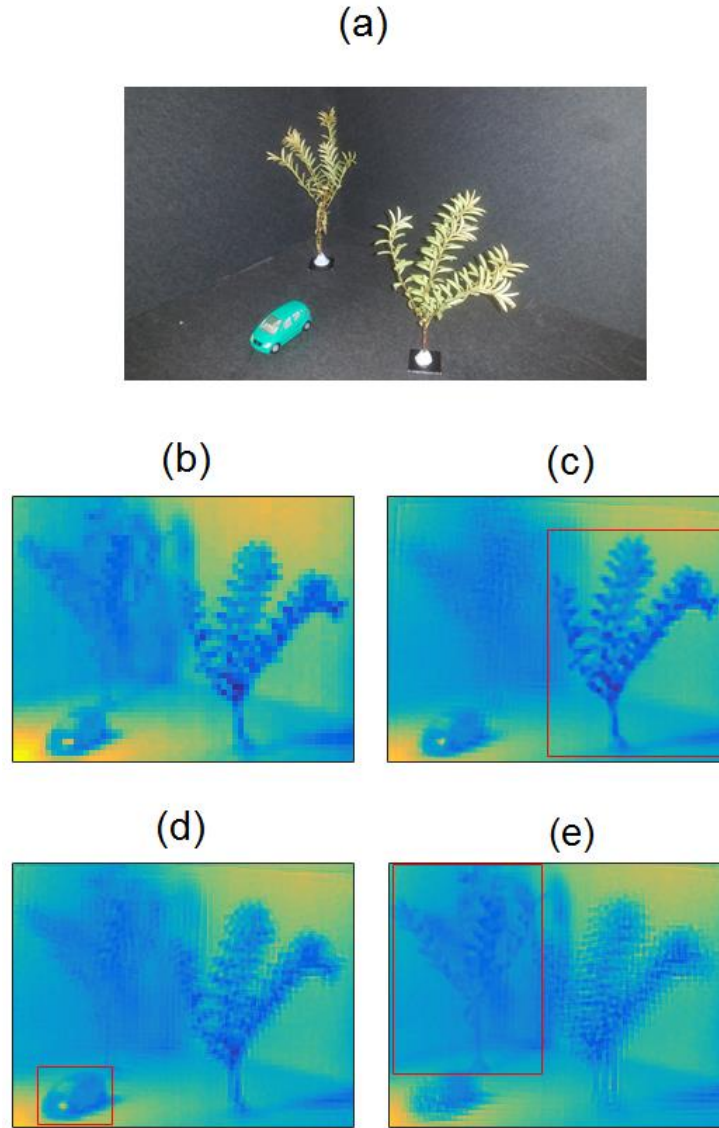


Figure 8. CIIR-SR results at different planes. Color image of the scene (a), and comparison of low resolution image from reference camera (b), super-resolved image at 0.820 m (c), 0.885 m (d), and 1.020 m (e).

In the third example application we report the recording of CIIR-SR video for 4D volumetric reconstruction (three spatial dimensions plus time), where the image can be digitally refocused with an improvement of the native resolution at any arbitrary plane in the video sequence. The images in Fig. 9 are taken from a video sequence and show: a single low-resolution image in in Fig. 9(a) while Figs 9(b) and (c) show CCIIR-SR reconstructions of the distal and proximal personnel and Figs. 7 (d) and (e) are expanded versions of the hand in Figs 9 (a) and (b) respectively highlighting the resolution enhancement and digital refocusing of CIIR-SR.

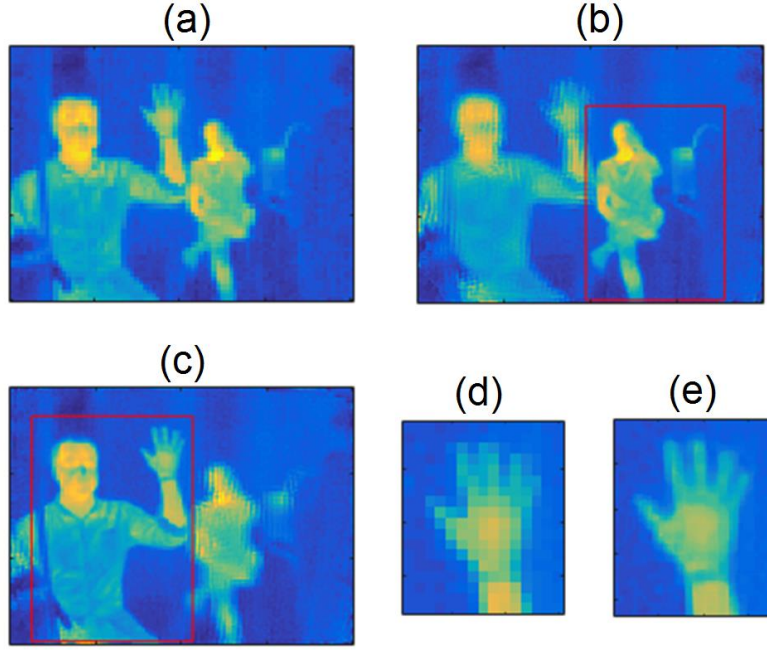


Figure 9. CIIR-SR results at different planes at video-rate. Comparison of low resolution image from reference camera (a), super-resolved image at 3 m (b), 6 m (c). A detailed comparison is shown for low resolution (d) and super-resolution (e).

4. Conclusion

We report the first demonstration of simultaneous super-resolution and computational integral-imaging reconstruction in the LWIR. This is achieved at video rate and low cost by synchronization of an array of low-cost, low-resolution LWIR cameras. This approach to high-resolution imaging also enables a fundamental reduction in both the track length and hence volume of an imaging system, while enabling cost reduction through the use of short-focal-length lenses replicated at low cost [30] from silicon or polyethylene.

We simultaneously demonstrate 3D imaging with a two-fold improvement in the angular resolution and hence four-fold improvement in space-bandwidth product. Therefore the proposed approach offers an agile route to high pixel count combined with the accepted capabilities of integral imaging. The future reduction in cost of LWIR detectors according to Moore's law, offers interesting routes to intelligent and agile imaging systems employing camera arrays to simultaneously demonstrate high space-bandwidth products and integral-imaging capabilities such as 3D imaging, ranging and recognition of obscured objects. Furthermore these camera arrays may be deployed conformal to host platforms.

Funding

This project has received funding from the European Union's Horizon 2020 research and innovation programme under grant agreement No 645114. G. C. also thanks the Leverhulme Trust for support.